Analytical Modeling of a Nanogap-Embedded FET for Application as a Biosensor

Ji-Min Choi, Jin-Woo Han, *Member, IEEE*, Sung-Jin Choi, and Yang-Kyu Choi

***Abstract*—An analytical model of a nanogap-embedded field-effect transistor, which is termed here simply as a biotransistor, is developed in this study. A surface potential model is attained by solving a 2-D Poisson equation with approximation of a parabolic potential profile along the channel depth. The analytical threshold voltage is then derived from the surface potential model to comprise the unique feature of the biotransistor, which acts as a biosensor. A shift of the threshold voltage was used as a metric to ascertain the sensitivity after the biomolecule interacts with the biotransistor. Various device parameters were investigated in the developed analytical model. The characteristic trend is supported and verified via a simulation. Hence, the proposed model can provide a useful guideline for the optimal design and fabrication of a biotransistor.**

***Index Terms*—Biotransistor, Dielectric-modulated field-effect transistor (DMFET), field-effect transistor (FET)-type biosensor, nanogap, nanogap-embedded FET, sensitivity, surface potential, threshold voltage, 2-D modeling, 2-D Poisson equation.**

I. INTRODUCTION

INTEREST in the use of a field-effect transistor (FET) for a range of biosensors has increased recently due to the numerous advantages that are achievable with such a design. These include miniaturization; the possibility for label-free electrical detection; high sensitivity; compatibility with traditional CMOS fabrication processes; the potential for mass-production; and feasibility for monolithic integration that combines a sensor, transducer, readout circuitry, and signal processor [1]–[16]. A large number of FET-type biosensors have been investigated in research related to nanowire FETs [1]–[5], ion-selective FETs [6]–[9], carbon nanotube FETs [10]–[12], extended-gate FETs [13], [14], and many other types. Embedding a nanogap in a traditional metal–oxide–semiconductor FET (MOSFET) structure was recently realized as a new type of biosensor based on FET technology [15]–[20]. This nanogap-embedded FET structure detects targeted biomolecules that are confined in the nanogap according to changes in electrical parameters, such as the threshold voltage [15]–[17] or the charge-pumping current [18]–[20]. The biomolecular detection method that uses the charge-pumping technique provides information pertaining to the specific binding through monitoring of the charge-pumping current. The first demonstrated nanogap-embedded FET, which is termed dielectric-modulated FET (DMFET), uses the shift of the threshold voltage as the biomolecular sensing parameter [15]. It includes a nanogap between the gate and gate oxide. The nanogap was created by carving some parts of the sacrificial layer preexisting between the gate and gate oxide. When biomolecules filled the nanogap, the threshold voltage V_T shifted due to the change of the dielectric constant K from unity, corresponding to air, to a certain number $(K > 1)$, corresponding to the biomolecules. Owing to this characteristic, the aforementioned FET was termed a DMFET (simply biotransistor). However, as other types of FET-type biosensors, an analytical model to describe ΔV_T has yet to be developed. Therefore, the development of an analytical model to describe the dielectric-modulation effect as a result of mutual interaction between the biomolecules and the biotransistor is required. In this study, as a sensing parameter in the biotransistor, the shift of the threshold voltage (ΔV_T) before and after immobilization of the biomolecules was used.

This work focuses on the development of an analytical V_T model of the biotransistor using a 2-D modeling technique to formulate a type of design guidance. The sensing parameter of the biotransistor is V_T, which is the most typical parameter among the numerous useful device parameters of the FET. The biotransistor is composed of three subparts of the gate dielectric. In order to suppress short-channel effects and minimize mobility degradation when a high-k gate dielectric is used for the entire region of the channel, a hybrid gate dielectric structure comprised a high-k component at the source edge, thermal oxide at the center, and a high-k component at the drain edge is deemed suitable. The proposed analytical model can also be applied to such a hybrid gate dielectric MOSFET.

II. STRUCTURE AND OPERATIONAL PRINCIPLE OF THE BIOTRANSISTOR

A schematic of the biotransistor is displayed in Fig. 1(a). The nanogap to induce a change of V_T is implemented at the edges of the gate in a silicon-on-insulator (SOI) substrate. A cross-sectional view [A-A' direction in Fig. 1(a)] of the biotransistor modeled in this paper is shown in Fig. 1(b). The operational principle of the biotransistor built with an n-channel is illustrated in Fig. 1(c) and (d). When the sacrificial layer (G_{bot})

Manuscript received March 9, 2010; revised August 20, 2010; accepted August 27, 2010. Date of publication October 7, 2010; date of current version November 19, 2010. This work was supported in part by the National Research and Development Program under Grant 2010-0002108 for the development of biomedical function monitoring biosensors and in part by the National Research Foundation of Korea funded by the Korean government under Grant 2010-0018931. The review of this paper was arranged by Editor A. M. Ionescu.

The authors are with the Department of Electrical Engineering, Korea Advanced Institute of Science and Technology, Daejeon 305-701, Korea (e-mail: ykchoi@ee.kaist.ac.kr).

Color versions of one or more of the figures in this paper are available online at http://ieeexplore.ieee.org.

Digital Object Identifier 10.1109/TED.2010.2076152

0018-9383/$26.00 © 2010 IEEE

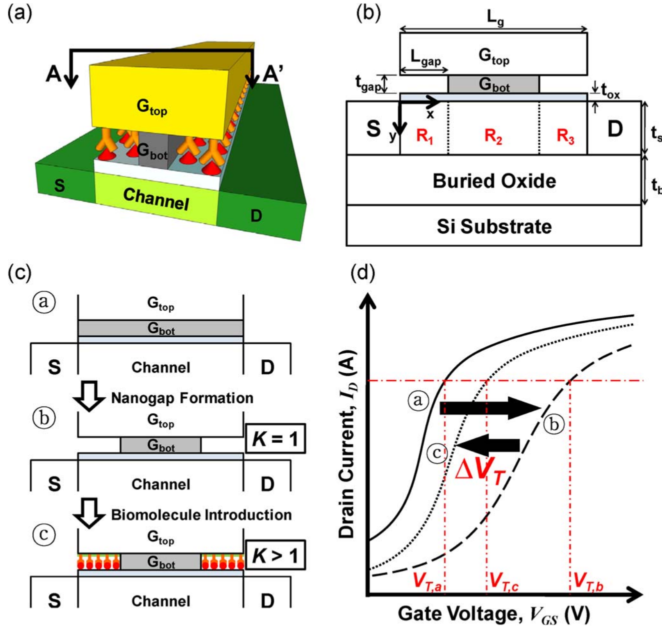

Fig. 1. Schematics of the biotransistor. (a) Three-dimensional schematic showing the biotransistor with biomolecules introduced in the nanogaps. (b) Cross-sectional view [A-A' direction in (a)] of the biotransistor. 2-D modeling is carried out in each of the three distinct regions. Regions 1 and 3 are underneath the nanogap. (c) Schematics to show the change of the dielectric constant due to nanogap formation and immobilization of the biomolecule inside the nanogap. (d) Operational principle of the biotransistor to show ΔV_T for each step depicted in (c).

in Fig. 1(c) was etched in part, air $(K = 1)$ inherently filled the nanogaps. Therefore, the effective dielectric constant of the gate dielectric, which is composed of the oxide $(K = 3.9)$ and air, was reduced. As a result, V_T increased from $V_{T,a}$ to $V_{T,b}$, as illustrated in Fig. 1(d). When biomolecules were introduced and immobilized in the nanogaps, the effective dielectric constant of the gate dielectric composed of the oxide $(K = 3.9)$ and the biomolecules $(K > 1)$ increased. As a consequence, V_T was reduced from $V_{T,b}$ to $V_{T,c}$. By sensing this value of ΔV_T $(= V_{T,b} - V_{T,c})$, the specific binding of biomolecules or interactions such as DNA hybridization or antigen–antibody reactions can be electrically identified without time-consuming and complicated labeling processes. This biotransistor sensing method has been experimentally demonstrated with the gate dielectric modulation effect [15]. However, as other types of FET-type biosensors, an analytical model to describe ΔV_T has not been developed. Therefore, analytical modeling of the V_T shift in the biotransistor is necessary to optimize device parameters such as the nanogap length $L_{\rm gap}$, nanogap thickness $t_{\rm gap}$, gate length L_g, gate oxide thickness $t_{\rm ox}$, channel thickness t_s, and the workfunctions of $G_{\rm top}$ and $G_{\rm bot}$ $(\phi_{M,\rm top}, \phi_{M,\rm bot})$.

III. Derivation of 2-D Surface Potential Model

Several studies have developed analytical threshold voltage models for modified structures from a traditional MOSFET [21], [22]. The procedure to attain the threshold voltage model of the biotransistor proceeds in the same manner. First, the channel potential distribution is derived by solving a 2-D Poisson equation through the use of proper assumptions and boundary conditions. The potential profile along the channel depth is approximated to the parabolic function in SOI devices [21]–[23]. Second, V_T is derived from the potential model of the biotransistor. V_T dependence on the device parameters is comprehensively investigated. Afterward, the modeling results are verified in comparison with simulation data.

The gate of the biotransistor consists of two layers $G_{\rm top}$ and $G_{\rm bot}$, as shown in Fig. 1(a). $G_{\rm bot}$ is a sacrificial layer for the formation of a lateral nanogap directly onto the gate oxide after a selective wet-etching process, whereas $G_{\rm top}$ acts as the main gate electrode. Details of the fabrication processes are available in the literature [15]. As the inversion charge density is assumed to be negligible in the subthreshold regime, the potential distribution $\phi(x, y)$ in the silicon channel is expressed as

$$\frac{d^2\phi(x,y)}{dx^2} + \frac{d^2\phi(x,y)}{dy^2} = \frac{qN_A}{\varepsilon_{\rm Si}} \tag{1}$$

for $0 \le x \le L_g$, $0 \le y \le t_s$, where q is the electronic charge, N_A is the doping concentration of the channel, $\varepsilon_{\rm Si}$ is the dielectric permittivity of silicon, L_g is the gate length, and t_s is the channel thickness. It should be noted that inaccuracy $\phi(x, y)$ can arise from the aforementioned approximation, i.e., only space charges (depletion charges) are considered. Nevertheless, this was traditionally used to obtain a closed form of $\phi(x, y)$. Due to the structural profile of the biotransistor, the channel region is divided into three regions R_j, as shown in Fig. 1(b), where $j = 1, 2, 3$ denotes the left-side nanogap, essential channel, and right-side nanogap region, respectively. Given that R_1 and R_3 are symmetric, the effective gate capacitance $C_{\rm eff}$ and flat-band voltage $V_{\rm FB}$ in R_1 and R_3 are represented by

$$C_{\rm eff} = \varepsilon_{\rm ox}\varepsilon_{\rm gap}/(\varepsilon_{\rm gap}t_{\rm ox} + \varepsilon_{\rm ox}t_{\rm gap})$$
$$V_{\rm FB,1} = V_{\rm FB,3} = \phi_{M,\rm top} - \phi_{\rm Si}$$

where $\varepsilon_{\rm ox}$ and $\varepsilon_{\rm gap}$ are the dielectric permittivity of the oxide and the nanogap-filling material, respectively; $t_{\rm ox}$ and $t_{\rm gap}$ are the thickness of the oxide and the nanogap-filling material (nanogap thickness), respectively; $\phi_{M,\rm top}$ is the workfunction of $G_{\rm top}$ (gold in the biotransistor, as reported in [15]); and $\phi_{\rm Si}$ is the workfunction of silicon. The latter value is known to be

$$\phi_{\rm Si} = \chi_{\rm Si} + E_g/2q + \phi_F$$

where $\chi_{\rm Si}$ is the electron affinity, E_g is the silicon energy band gap, and ϕ_F is the difference between the extrinsic and intrinsic Fermi potential level, i.e., $\phi_F = kT/q \ln(N_A/n_i)$. The gate capacitance $C_{\rm ox}$ and flat-band voltage $V_{\rm FB}$ in R_2 are correspondingly written as

$$C_{\rm ox} = \varepsilon_{\rm ox}/t_{\rm ox} \quad \text{and} \quad V_{\rm FB,2} = \phi_{M,\rm bot} - \phi_{\rm Si}$$

where $\phi_{M,\rm bot}$ is the workfunction of $G_{\rm bot}$ (chromium in the biotransistor, as presented in [15]).

A parabolic assumption along the channel depth has been commonly used as a modeling technique for fully depleted SOI devices after Young proved its validity for the first time [23].

The parabolic approximated potential distribution $\phi(x,y)$ for each region is given by

$$\phi_j(x,y) = \phi_{S,j}(x) + c_{a,j}(x)y + c_{b,j}(x)y^2 \tag{2}$$

where j denotes each region, $\phi_{S,j}$ is the potential at the channel surface, i.e., $\phi_j(x,0)$, and $c_{a,j}$ and $c_{b,j}$ are arbitrary coefficients determined as a function of x only. The coefficients $c_{a,j}$ and $c_{b,j}$ are calculated from the boundary conditions that satisfy the continuity of the electric displacement at the interface of the oxide and silicon channel. These are

$$\begin{cases} \left.\frac{d\phi_j(x,y)}{dy}\right|_{y=0} = \frac{C_j}{\varepsilon_{\rm Si}}\left(\phi_{S,j}(x) - V_{GS} + V_{{\rm FB},j}\right) \\ \left.\frac{d\phi_j(x,y)}{dy}\right|_{y=t_s} = -\frac{C_B}{\varepsilon_{\rm Si}}\left(\phi_B(x) - V_{\rm SUB} + V_{{\rm FB},b}\right) \end{cases} \tag{3}$$

where V_{GS} is the gate-to-source bias, $V_{\rm SUB}$ is the substrate bias, $V_{{\rm FB},b}$ is the flat-band voltage at the back-channel, $\phi_B = \phi(x,t_s)$ is the potential at the back-channel surface, $C_B = \varepsilon_{\rm ox}/t_b$ is the back-channel oxide capacitance, $C_1 = C_3 = C_{\rm eff}$, and $C_2 = C_{\rm ox}$. Plugging $\phi(x,y)$ into a 2-D Poisson equation (1), the equation is rewritten in the form of a 1-D second-order differential equation, i.e.,

$$\frac{d^2\phi_{S,j}(x)}{dx^2} - \alpha_j\phi_{S,j}(x) = \beta_j \tag{4}$$

where

$$\begin{aligned} \alpha_1 = \alpha_3 &= \frac{2(1 + C_{\rm eff}/C_S + C_{\rm eff}/C_B)}{t_s^2(1+2C_S/C_B)} \\ \beta_1 = \beta_3 &= \frac{qN_A}{\varepsilon_{\rm Si}} - 2(V_{GS} - V_{\rm FB,1})\left(\frac{C_{\rm eff}/C_S + C_{\rm eff}/C_B}{t_s^2(1+2C_S/C_B)}\right) \\ &\quad - 2(V_{\rm SUB} - V_{{\rm FB},b})\left(\frac{1}{t_s^2(1+2C_S/C_B)}\right) \\ \alpha_2 &= \frac{2(1 + C_{\rm ox}/C_S + C_{\rm ox}/C_B)}{t_s^2(1+2C_S/C_B)} \\ \beta_2 &= \frac{qN_A}{\varepsilon_{\rm Si}} - 2(V_{GS} - V_{\rm FB,2})\left(\frac{C_{\rm ox}/C_S + C_{\rm ox}/C_B}{t_s^2(1+2C_S/C_B)}\right) \\ &\quad - 2(V_{\rm SUB} - V_{{\rm FB},b})\left(\frac{1}{t_s^2(1+2C_S/C_B)}\right) \end{aligned}$$

and where the channel capacitance is written as $C_S = \varepsilon_{\rm Si}/t_s$. If $L_{\rm gap}$ tends to be zero, regions R_1 and R_3 disappear, i.e., there are no nanogaps. Thus, the preceding equations are reduced to a simple form, which is identical to the model reported in [23]. The general solution of (4) for each region is represented as

$$\phi_{S,j}(x) = A_j\exp(\lambda_j x) + B_j\exp(-\lambda_j x) + \sigma_j \tag{5}$$

where $\lambda_1 = \lambda_3 = \sqrt{\alpha_1}$, $\sigma_1 = \sigma_3 = -\beta_1/\alpha_1$, $\lambda_2 = \sqrt{\alpha_2}$, and $\sigma_2 = -\beta_2/\alpha_2$. The coefficients A_j and B_j are derived from the boundary conditions satisfying continuity of the potential and electric field between adjacent regions. The built-in potential at the source/drain edge and $V_{\rm DS}$ (drain-to-source bias) are also considered. These boundary conditions are represented as

$$\begin{cases} \phi_{S,1}(L_1) = \phi_{S,2}(L_1) \\ \phi_{S,2}(L_1+L_2) = \phi_{S,3}(L_1+L_2) \\ \left.\frac{d\phi_{S,1}(x)}{dx}\right|_{x=L_1} = \left.\frac{d\phi_{S,2}(x)}{dx}\right|_{x=L_1} \\ \left.\frac{d\phi_{S,2}(x)}{dx}\right|_{x=L_1+L_2} = \left.\frac{d\phi_{S,3}(x)}{dx}\right|_{x=L_1+L_2} \\ \phi_{S,1}(0) = V_{\rm bi} \\ \phi_{S,3}(L_g) = V_{\rm bi} + V_{\rm DS} \end{cases} \tag{6}$$

where $V_{\rm bi} = (kT/q)\ln(N_AN_D/n_i^2)$ is the built-in potential across the channel–source junction, and N_D is the source/drain doping concentration. For simplicity, $L_{\rm gap}$ is replaced by L_1; hence, the length of the essential channel $L_2 = L_g - 2L_1$ is defined. The calculated coefficients A_j and B_j are summarized in the Appendix.

IV. Derivation of Threshold Voltage Model

The minimum surface potential was used as a reference to define V_T because it serves as a criterion of the flow current, i.e., the barrier height. As there are three channel regions controlled by different physical device parameters, i.e., $\varepsilon_{\rm ox}$, $\varepsilon_{\rm gap}$, $t_{\rm ox}$, $t_{\rm gap}$, $\phi_{M,\rm top}$, and $\phi_{M,\rm bot}$, the potential minimum values of each region should differ from each other. Accordingly, the V_T value of each region ($V_{T,j}, j = 1,2,3$) should also be different. Under a nominal n-channel MOSFET operation, the drain is positively biased, compared to the source. Hence, the potential minimum of R_3 is always larger than that of R_1. Therefore, it is unnecessary to find V_T at R_3 ($V_{T,3}$). The potential minimum between R_1 and R_2 depends on the nanogap length, implying that both $V_{T,1}$ and $V_{T,2}$ must be solved. However, $L_{\rm gap}$ should be sufficiently large in order to create a highly sensitive biotransistor. In addition, supplementary capacitance components related with the two side walls of the $G_{\rm bot}$ layer become negligible as $L_{\rm gap}$ becomes larger. Therefore, the use of analytical modeling that considers each of the three regions as separate parallel-plate capacitors is an effective method. In this condition, $V_{T,1}$ plays a crucial role in sensing the biomolecules. Thus, the potential minimum in R_1 tends to be dominant in controlling the total V_T because $V_{T,2}$ is no longer an important parameter for device analysis. In consideration of these necessary conditions to make the biotransistor highly sensitive, the potential minimum is expressed as

$$\phi_{S,\min} = 2\sqrt{A_1B_1} + \sigma_1. \tag{7}$$

V_T is defined as the value of V_{GS} for which $\phi_{S,\min} = 2\phi_F$. This is solved as

$$V_T = \frac{-\psi_b + \sqrt{\psi_b^2 - 4\Omega_a\psi_c}}{2\Omega_a} \tag{8}$$

where Ω_a, ψ_b, and ψ_c are summarized in the Appendix. It is worthwhile to note that $V_{T,2}$ is more important than $V_{T,1}$ only when the nanogap length is below several tens of nanometers. This fact is verified by both the analytical $V_{T,2}$ model and the simulation. Equation (8) and the V_T model in [21] become

TABLE I
NOMINAL DEVICE DIMENSIONS USED FOR THE VERIFICATION OF THE ANALYTICAL MODEL WITH THE AID OF THE SILVACO SIMULATOR IN THE BIO-TRANSISTOR

Parameter	Symbol	Value
Gate length	L_g	1000 nm
Silicon film doping	N_A	10^{17} cm^{-3}
S/D doping	N_D	10^{20} cm^{-3}
Channel thickness	t_s	50 nm
Gate oxide thickness	t_{ox}	10 nm
Nanogap length	L_{gap}	400 nm
Nanogap thickness	t_{gap}	15 nm
Buried oxide thickness	t_b	300 nm
Gate top layer (G_{top}) workfunction	$\phi_{M,top}$	5.1 V (for Au)
Gate bottom layer (G_{bot}) workfunction	$\phi_{M,bot}$	4.5 V (for Cr)

identical expressions when $L_{\rm gap}$ in this work is considered to be half of the gate length, and L_2 in [21] is set to zero, causing the structures of both devices to return to a conventional SOI MOSFET structure [23].

The sensitivity of the biotransistor is characterized by ΔV_T before and after immobilization of the biomolecules. Thereby, it is defined as

$$\Delta V_T = V_T(\varepsilon_{\rm gap} = 1) - V_T(\varepsilon_{\rm gap} = K). \quad (9)$$

This closed form of ΔV_T is useful for a comprehensive understanding of the biotransistor in terms of device parameter changes.

V. RESULTS AND DISCUSSION

The device parameters used for the analytical model of the biotransistor are summarized in Table I. The surface potential distribution along the channel was plotted for various values of $L_{\rm gap}$ in Fig. 2 with the aid of the analytical model. Distortion of the potential profile is clearly observed under the nanogap region, whereas no deformation of the potential profile is observed in a device without a nanogap device ($L_{\rm gap} = 0$). $V_{\rm DS}$ is biased at 0.05 V, and V_{GS} is biased at the onset of V_{T0}, which is the threshold voltage of the initial device without nanogaps. It should be noted that potential distortion becomes more significant as $L_{\rm gap}$ increases. Therefore, a sufficiently long $L_{\rm gap}$ is preferred for enhancement of the sensitivity of the biotransistor because V_T stemming from the potential minimum is a crucial parameter in determining the detection sensitivity.

In Fig. 3, the calculated ΔV_T is compared to the simulated result for different values of $L_{\rm gap}$ by employment of the SILVACO tool. Two different dielectric constants of the biomolecules to fill the nanogaps are used for verification of the model. A dielectric constant of 2 was chosen for biomaterials with a low dielectric constant. A value of 12 was chosen for

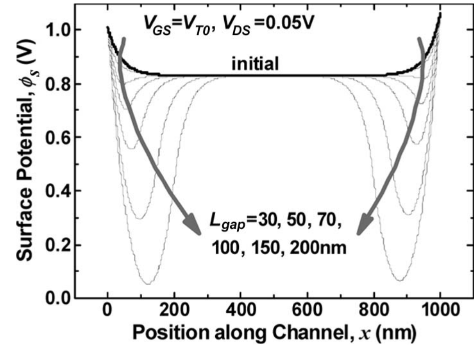

Fig. 2. Surface potential distribution of a conventional MOSFET without a nanogap ($L_{\rm gap} = 0$) and the biotransistor with various nanogap lengths. The distortion of the potential distribution is noticeable under the nanogap region. The increment of $L_{\rm gap}$ causes more significant potential deformation in the nanogap region.

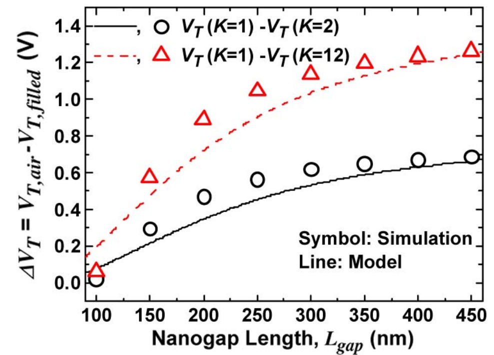

Fig. 3. Dependence of the ΔV_T value on the nanogap length $L_{\rm gap}$. A longer $L_{\rm gap}$ results in higher sensitivity. ΔV_T starts to become saturated when $L_{\rm gap}$ exceeds a certain value.

those with a high dielectric. As expected, a larger value of ΔV_T was observed with a longer $L_{\rm gap}$. In addition, the increment of $L_{\rm gap}$ resulted in higher sensitivity (ΔV_T), which is very attractive for application as a biosensor. It is important to note that saturation of ΔV_T begins when $L_{\rm gap}$ exceeds a certain value. This gives a clear indication that $L_{\rm gap}$ does not have to be as large as possible. An $L_{\rm gap}$ of 400 nm is acceptable to show reasonable sensitivity. Some discrepancy between the modeled and simulated data may arise from ambiguity in the definition of V_T at the potential minimum. However, this does not hamper understanding of the parametric dependency of the biotransistor.

Fig. 4 reflects the optimal size of the biotransistor. In Fig. 4(a), the transfer characteristics of the biotransistor for a short versus a long gate length are compared. The ratio of $L_{\rm gap}$ to L_g is fixed at 0.4 to form a substantial gate electrode without stiction of $G_{\rm top}$ against $G_{\rm bot}$. In the case of a short gate length, there is no significant ΔV_T, revealing that it is not appropriate for a biosensor. In contrast, there is a notable value of ΔV_T in a device with a long gate length. In the field of biosensors, device size and scaling are not major concerns because the transducer and readout circuitry size is much larger than the size of the biosensor itself. In Fig. 4(b), the ΔV_T characteristic is examined as a function of L_g. ΔV_T is insensitive to L_g as long as $L_{\rm gap}$ is fixed at a reasonable value. This trend reveals that the biotransistor may not experience process variability.

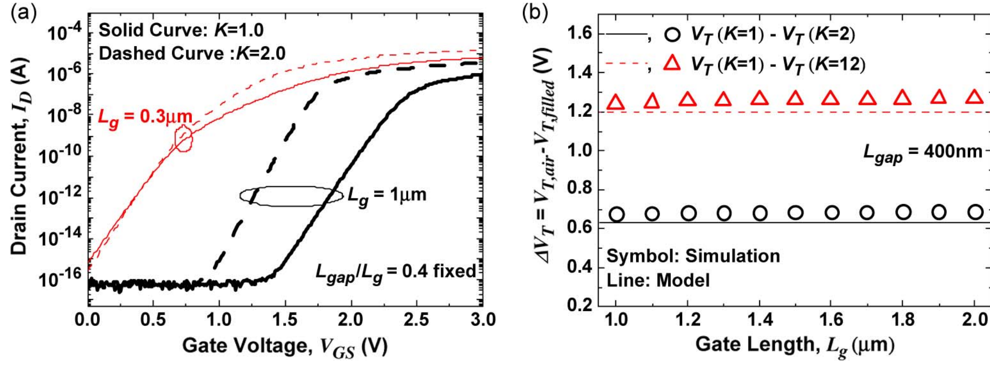

Fig. 4. (a) Transfer characteristics of the biotransistor for different gate lengths with a fixed ratio of L_{gap} to L_g. Aggressive scaling of L_g is not appropriate for the biotransistor. (b) ΔV_T versus L_g. The L_g parameter does not greatly influence the sensitivity of the biotransistor when L_{gap} is kept constant.

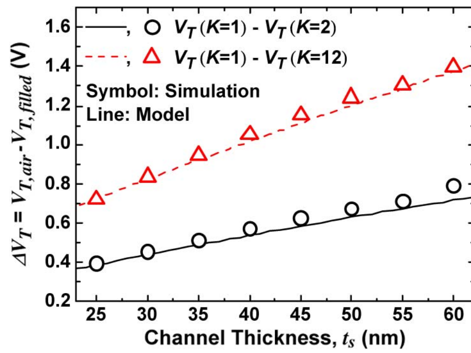

Fig. 5. Dependence of ΔV_T on the channel thickness t_s. A thicker t_s is preferred for high sensitivity.

Additionally, it supports that the absolute value of L_{gap} is the key element to determine sensitivity rather than the ratio of L_{gap} to L_g. This is because $V_{T,1}$ at R_1 represents the majority of the total V_T, which is composed of $V_{T,1}$, $V_{T,2}$, and $V_{T,3}$, regardless of the length of R_2 on the condition that the value of L_{gap} is larger than a certain number. In terms of the process, L_g should be at least slightly longer than twice the distance of L_{gap} to avoid pattern lift-off during the wet-etching process to carve the sacrificial layer, as nanogaps are formed both at the drain and source sides. For example, L_g of 1 μm and L_{gap} of 400 nm are feasible for a biotransistor to be used as a biosensor without sacrifice of the mechanical stability in G_{top}.

The thickness of the channel in SOI devices can be an important factor that affects the characteristics of the device. Fig. 5 shows the tendency in which ΔV_T linearly increases as the channel thickness becomes thicker. The modeled data show good agreement with the simulated result. An approximate sensitivity improvement of 70% is expected when the channel thickness doubles. This trend is attributed to the increased depletion charges in the thickened channel. This implies that the entire depletion region in a fully depleted SOI device contributes to the biomolecular detection characteristics.

The thickness of the gate oxide is also a crucial parameter in the control of V_T. Thermally grown oxide is preferred to ensure stable device performance, as demonstrated in a recent study [16]. The effect of the thickness of the gate oxide was also investigated, as shown in Fig. 6(a). Detection sensitivity (ΔV_T) is independent of the gate oxide thickness, regardless of

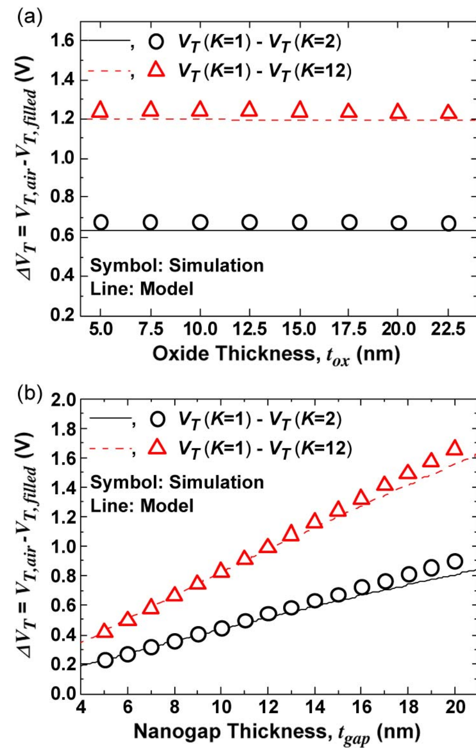

Fig. 6. (a) Dependence of ΔV_T on the oxide thickness t_{ox}. The parameter t_{ox} does not greatly influence the sensitivity of the biotransistor. (b) Dependence of ΔV_T on the nanogap thickness t_{gap}.

the dielectric constant of the biomolecules. This implies that the gate oxide thickness is a parameter that can be decoupled from other device parameters in maximizing the performance of a MOSFET without specific consideration of the biomolecules. On the other hand, it supports that the sensitivity is entirely governed not by the gate oxide thickness but by the nanogap dimensions. Another confirmation of this fact is shown in Fig. 6(b). ΔV_T linearly increases as t_{gap} becomes thicker. For simplicity, it is assumed that the nanogap is completely filled by biomolecules. As expected, a larger nanogap thickness results in a larger value of ΔV_T. However, the nanogap thickness should be adjusted to the size of the targeted biomolecules. It should be comparable or thick enough to accommodate the targeted biomolecules.

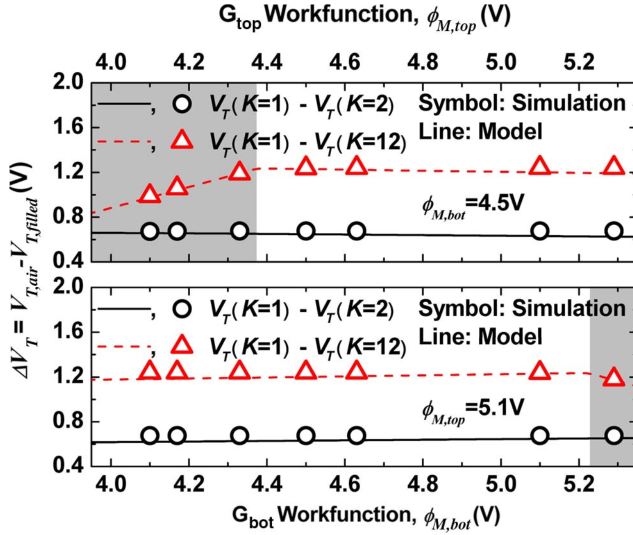

Fig. 7. Dependence of ΔV_T on the workfunction in the hybrid gate electrode. Selection of a workfunction of $G_{\rm top}$ higher than that of $G_{\rm bot}$ assures a robust ΔV_T, which is not affected by the sacrificial layer of $G_{\rm bot}$.

Thus far, comprehensive studies of the presented model have been investigated for a nanogap-embedded FET structure with gold as the $G_{\rm top}$ layer and chromium as the $G_{\rm bot}$ layer. However, it should be recalled that the primary purpose of $G_{\rm bot}$ is to serve as a sacrificial layer to form the nanogap, whereas that of $G_{\rm top}$ is to provide binding sites to accommodate biomolecules with high selectivity to inhibit the biomolecules from being immobilized onto other nondesigned surfaces such as the source, drain, gate oxide, and $G_{\rm bot}$. Accordingly, the $G_{\rm top}$ material whose surface is more likely to bind with target biomolecules is preferred. In terms of biocompatibility, gold is attractive for $G_{\rm top}$ due to its excellent biostability and chemical stability. Chromium is highly appropriate for $G_{\rm bot}$ because it can serve as both a sacrificial layer and a glue layer that holds the gold onto the oxide. However, sufficient etching selectivity against the $G_{\rm top}$ material is a prerequisite for the material for $G_{\rm bot}$. Hence, selection of the gate material must be properly optimized.

In terms of device operation, it is desirable that the workfunction of this hybrid gate electrode does not impact the value of ΔV_T significantly. Fig. 7 exhibits how ΔV_T depends on the material property of the $G_{\rm top}$ and $G_{\rm bot}$ layer, i.e., the gate workfunction. In the proposed structure, there are three regions that show different workfunctions: $\phi_{M,\rm top}$ is the gate workfunction at R_1 and R_3, whereas $\phi_{M,\rm bot}$ is the gate workfunction at R_2. The figure in the upper part of Fig. 7 shows the impact of $\phi_{M,\rm top}$ on ΔV_T when $\phi_{M,\rm bot}$ is fixed, whereas the lower part of this figure shows the impact of $\phi_{M,\rm bot}$ on ΔV_T when $\phi_{M,\rm top}$ is fixed. As long as $\phi_{M,\rm top}$ is larger than $\phi_{M,\rm bot}$, ΔV_T is insensitive to the workfunction of the hybrid gate electrode on the biotransistor. Therefore, the selection of gate materials must be done to ensure that $\phi_{M,\rm top}$ is larger than $\phi_{M,\rm bot}$. As gold is known to have a workfunction that is approximately 0.6 V higher than chromium, the proposed hybrid gate structure of gold–chromium in [15] can ensure a stable value of ΔV_T.

VI. Conclusion

The analytical surface potential distribution of a biotransistor has been investigated, and an analytical threshold voltage model has been derived from the potential model. The proposed threshold voltage model has comprehensively explained the unique characteristics of the biotransistor and showed good agreement with the simulated data. It has provided how each device parameter affects the sensitivity extrinsically. The proposed analytical model can provide a useful guideline for the optimization of device dimensions to maximize sensitivity of biotransistors.

Appendix

The coefficients A_j and B_j in (5) are represented as

$$A_1 = \frac{2V_{DS} + (V_{bi} - \sigma_1)\chi_A + 2(\sigma_1 - \sigma_2)P}{Q} \tag{A-1}$$

$$B_1 = \frac{-2V_{DS} - (V_{bi} - \sigma_1)\chi_B - 2(\sigma_1 - \sigma_2)P}{Q} \tag{A-2}$$

$$\begin{aligned} A_2 =& \frac{1}{2}(\sigma_1 - \sigma_2)\exp(-\lambda_2 L_1) \\ &+ \frac{1}{2}\left(1 + \frac{\lambda_1}{\lambda_2}\right)\exp\left((\lambda_1 - \lambda_2)L_1\right)A_1 \\ &+ \frac{1}{2}\left(1 - \frac{\lambda_1}{\lambda_2}\right)\exp\left(-(\lambda_1 + \lambda_2)L_1\right)B_1 \end{aligned} \tag{A-3}$$

$$\begin{aligned} B_2 =& \frac{1}{2}(\sigma_1 - \sigma_2)\exp(\lambda_2 L_1) \\ &+ \frac{1}{2}\left(1 - \frac{\lambda_1}{\lambda_2}\right)\exp\left((\lambda_1 + \lambda_2)L_1\right)A_1 \\ &+ \frac{1}{2}\left(1 + \frac{\lambda_1}{\lambda_2}\right)\exp\left(-(\lambda_1 - \lambda_2)L_1\right)B_1 \end{aligned} \tag{A-4}$$

$$\begin{aligned} A_3 =& \frac{1}{2}(\sigma_2 - \sigma_1)\exp\left(-\lambda_1(L_1 + L_2)\right) \\ &+ \frac{1}{2}\left(1 + \frac{\lambda_2}{\lambda_1}\right)\exp\left((\lambda_2 - \lambda_1)(L_1 + L_2)\right)A_2 \\ &+ \frac{1}{2}\left(1 - \frac{\lambda_2}{\lambda_1}\right)\exp\left(-(\lambda_2 + \lambda_1)(L_1 + L_2)\right)B_2 \end{aligned} \tag{A-5}$$

$$\begin{aligned} B_3 =& \frac{1}{2}(\sigma_2 - \sigma_1)\exp\left(\lambda_1(L_1 + L_2)\right) \\ &+ \frac{1}{2}\left(1 - \frac{\lambda_2}{\lambda_1}\right)\exp\left((\lambda_2 + \lambda_1)(L_1 + L_2)\right)A_2 \\ &+ \frac{1}{2}\left(1 + \frac{\lambda_2}{\lambda_1}\right)\exp\left(-(\lambda_2 - \lambda_1)(L_1 + L_2)\right)B_2 \end{aligned} \tag{A-6}$$

where

$$\begin{aligned} \chi_A =& 2 - 2\exp(-2\lambda_1 L_1)\cosh(\lambda_2 L_2) \\ &+ \left(\frac{\lambda_1}{\lambda_2} + \frac{\lambda_2}{\lambda_1}\right)\exp(-2\lambda_1 L_1)\sinh(\lambda_2 L_2) \\ &+ \left(\frac{\lambda_1}{\lambda_2} - \frac{\lambda_2}{\lambda_1}\right)\sinh(\lambda_2 L_2) \end{aligned} \tag{A-7}$$

$$\chi_B = 2 - 2\exp(2\lambda_1 L_1)\cosh(\lambda_2 L_2) - \left(\frac{\lambda_1}{\lambda_2} + \frac{\lambda_2}{\lambda_1}\right)\exp(2\lambda_1 L_1)\sinh(\lambda_2 L_2) - \left(\frac{\lambda_1}{\lambda_2} - \frac{\lambda_2}{\lambda_1}\right)\sinh(\lambda_2 L_2) \quad \text{(A-8)}$$

$$P = \cosh(\lambda_1 L_1)\left(1 - \cosh(\lambda_2 L_2)\right) - (\lambda_2/\lambda_1)\sinh(\lambda_1 L_1)\sinh(\lambda_2 L_2) \quad \text{(A-9)}$$

$$Q = 4\sinh(2\lambda_1 L_1)\cosh(\lambda_2 L_2) + 2\left(\frac{\lambda_1}{\lambda_2} + \frac{\lambda_2}{\lambda_1}\right)\cosh(2\lambda_1 L_1)\sinh(\lambda_2 L_2) + 2\left(\frac{\lambda_1}{\lambda_2} - \frac{\lambda_2}{\lambda_1}\right)\sinh(\lambda_2 L_2). \quad \text{(A-10)}$$

The complicated expressions of the coefficients Ω_a, ψ_b, and ψ_c in (8) are briefly represented as

$$\Omega_a = 4\tau_A\tau_B - S_1^2 Q^2 \quad \text{(A-11)}$$

$$\psi_b = 4(\tau_A V_{DS,B} + \tau_B V_{DS,A}) - 2S_1 Q^2 (u_1 - 2\phi_F) \quad \text{(A-12)}$$

$$\psi_c = 4V_{DS,A}V_{DS,B} - Q^2(u_1 - 2\phi_F)^2 \quad \text{(A-13)}$$

where

$$S_1 = \frac{C_{\text{eff}}/C_S + C_{\text{eff}}/C_B}{1 + C_{\text{eff}}/C_S + C_{\text{eff}}/C_B} \quad \text{(A-14)}$$

$$S_2 = \frac{C_{\text{ox}}/C_S + C_{\text{ox}}/C_B}{1 + C_{\text{ox}}/C_S + C_{\text{ox}}/C_B} \quad \text{(A-15)}$$

$$u_1 = (V_{\text{SUB}} - V_{\text{FB},b})\left(\frac{1}{1 + C_{\text{eff}}/C_S + C_{\text{eff}}/C_B}\right) - \frac{qN_A t_s^2 (1 + 2C_S/C_B)}{2\varepsilon_{\text{Si}}(1 + C_{\text{eff}}/C_S + C_{\text{eff}}/C_B)} - S_1 V_{\text{FB},1} \quad \text{(A-16)}$$

$$u_2 = (V_{\text{SUB}} - V_{\text{FB},b})\left(\frac{1}{1 + C_{\text{ox}}/C_S + C_{\text{ox}}/C_B}\right) - \frac{qN_A t_s^2 (1 + 2C_S/C_B)}{2\varepsilon_{\text{Si}}(1 + C_{\text{ox}}/C_S + C_{\text{ox}}/C_B)} - S_2 V_{\text{FB},2} \quad \text{(A-17)}$$

$$\tau_A = 2(S_1 - S_2)P - S_1\chi_A \quad \text{(A-18)}$$

$$V_{DS,A} = 2V_{DS} + (V_{\text{bi}} - u_1)\chi_A + 2(u_1 - u_2)P \quad \text{(A-19)}$$

$$\tau_B = -2(S_1 - S_2)P + S_1\chi_B \quad \text{(A-20)}$$

$$V_{DS,B} = -2V_{DS} - (V_{\text{bi}} - u_1)\chi_B - 2(u_1 - u_2)P. \quad \text{(A-21)}$$

REFERENCES

[1] Y. Cui, Q. Wei, H. Park, and C. M. Lieber, "Nanowire nanosensors for highly sensitive and selective detection of biological and chemical species," *Science*, vol. 293, no. 5533, pp. 1289–1292, Aug. 2001.

[2] E. Stern, J. F. Klemic, D. A. Routenberg, P. N. Wyrembak, D. B. Turner-Evans, A. D. Hamilton, D. A. LaVan, T. M. Fahmy, and M. A. Reed, "Label-free immunodetection with CMOS-compatible semiconducting nanowires," *Nature*, vol. 445, no. 7127, pp. 519–523, Feb. 2007.

[3] Z. Li, Y. Chen, X. Li, T. I. Kamins, K. Nauka, and R. S. Williams, "Sequence-specific label-free DNA sensors based on silicon nanowires," *Nano Lett.*, vol. 4, no. 2, pp. 245–247, Feb. 2004.

[4] J. Hahm and C. M. Lieber, "Direct ultrasensitive electrical detection of DNA and DNA sequence variations using nanowire nanosensors," *Nano Lett.*, vol. 4, no. 1, pp. 51–54, Jan. 2004.

[5] M. Curreli, R. Zhang, F. N. Ishikawa, H.-K. Chang, R. J. Cote, C. Zhou, and M. E. Thompson, "Real-time, label-free detection of biological entities using nanowire-based FETs," *IEEE Trans. Nanotechnol.*, vol. 7, no. 6, pp. 651–667, Nov. 2008.

[6] M. J. Schöning and A. Poghossian, "Recent advances in biologically sensitive field-effect transistors (BioFETs)," *Analyst*, vol. 127, no. 9, pp. 1137–1151, Sep. 2002.

[7] P. Bergveld, "Thirty years of ISFETOLOGY: What happened in the past 30 years and what may happen in the next 30 years," *Sens. Actuators B, Chem.*, vol. 88, no. 1, pp. 1–20, Jan. 2003.

[8] K. Y. Park, S. B. Choi, M. Lee, B. K. Sohn, and S. Y. Choi, "ISFET glucose sensor system with fast recovery characteristics by employing electrolysis," *Sens. Actuators B, Chem.*, vol. 83, no. 1–3, pp. 90–97, Mar. 2002.

[9] A. Phogossian, J. Schoning, P. Schroth, A. Simonis, and H. Luth, "An ISFET-based penicillin sensor with high sensitivity, low detection limit and long lifetime," *Sens. Actuators B, Chem.*, vol. 76, no. 1–3, pp. 519–526, Jun. 2001.

[10] P. Qi, O. Vermesh, M. Grecu, A. Javey, Q. Wang, H. Dai, S. Peng, and K. J. Cho, "Toward large arrays of multiplex functionalized carbon nanotube sensors for highly sensitive and selective molecular detection," *Nano Lett.*, vol. 3, no. 3, pp. 347–351, Mar. 2003.

[11] A. Star, E. Tu, J. Niemann, J. P. Gabriel, C. S. Joiner, and C. Valcke, "Label-free detection of DNA hybridization using carbon nanotube network field-effect transistors," *Proc. Nat. Acad. Sci. USA*, vol. 103, no. 4, pp. 921–926, Jan. 2006.

[12] M. T. Martinez, Y.-C. Tseng, N. Ormategui, I. Loinaz, R. Eritja, and J. Bokor, "Label-free DNA biosensors based on functionalized carbon nanotube field effect transistors," *Nano Lett.*, vol. 9, no. 2, pp. 530–536, Feb. 2009.

[13] J.-C. Chen, J.-C. Chou, T.-P. Sun, and S.-K. Hsiung, "Portable urea biosensor based on the extended-gate field effect transistor," *Sens. Actuators B, Chem.*, vol. 91, no. 1–3, pp. 180–186, Jun. 2003.

[14] D.-S. Kim, J.-E. Park, J.-K. Shin, P. K. Kim, G. Lim, and S. Shoji, "An extended gate FET-based biosensor integrated with a Si microfluidic channel for detection of protein complexes," *Sens. Actuator B, Chem.*, vol. 117, no. 2, pp. 488–494, Oct. 2006.

[15] H. Im, X.-J. Huang, B. Gu, and Y.-K. Choi, "A dielectric-modulated field-effect transistor for biosensing," *Nat. Nanotechnol.*, vol. 2, no. 7, pp. 430–434, Jul. 2007.

[16] B. Gu, T. J. Park, J.-H. Ahn, X.-J. Huang, S. Y. Lee, and Y.-K. Choi, "Nanogap field-effect transistor biosensors for electrical detection of avian influenza," *Small*, vol. 5, no. 21, pp. 2407–2412, Nov. 2009.

[17] C.-H. Kim, C. Jung, H. G. Park, and Y.-K. Choi, "Novel dielectric-modulated field-effect transistor for label-free DNA detection," *Biochip J.*, vol. 2, no. 2, pp. 127–134, Jun. 2008.

[18] S. Kim, J.-H. Ahn, T. J. Park, S. Y. Lee, and Y.-K. Choi, "A biomolecular detection method based on charge pumping in a nanogap embedded field-effect-transistor biosensor," *Appl. Phys. Lett.*, vol. 94, no. 24, p. 243 903, Jun. 2009.

[19] S. Kim, J.-H. Ahn, T. J. Park, S. Y. Lee, and Y.-K. Choi, "Charge pumping technique to analyze the effect of intrinsically retained charges and extrinsically trapped charges in biomolecules by use of a nanogap embedded biotransistor," *Appl. Phys. Lett.*, vol. 96, no. 5, p. 053 701, Feb. 2010.

[20] S. Kim, J.-H. Ahn, T. J. Park, S. Y. Lee, and Y.-K. Choi, "Comprehensive study of a detection mechanism and optimization strategies to improve sensitivity in a nanogap-embedded biotransistor," *J. Appl. Phys.*, vol. 107, no. 11, p. 114 705, Jun. 2010.

[21] M. J. Kumar and A. Chaudhry, "Two-dimensional analytical modeling of fully depleted DMG SOI MOSFET and evidence for diminished SCEs," *IEEE Trans. Electron Devices*, vol. 51, no. 4, pp. 569–574, Apr. 2004.

[22] A. O. Adan, K. Higashi, and Y. Fukushima, "Analytical threshold voltage model for ultrathin SOI MOSFETs including short-channel and floating-body effects," *IEEE Trans. Electron Devices*, vol. 46, no. 4, pp. 729–737, Apr. 1999.

[23] K. K. Young, "Short-channel effect in fully depleted SOI MOSFETs," *IEEE Trans. Electron Devices*, vol. 36, no. 2, pp. 399–402, Feb. 1989.

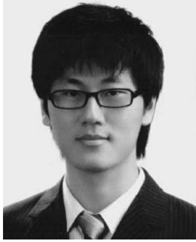

Ji-Min Choi received the B.S. degree, in 2009, from Korea Advanced Institute of Science and Technology, Daejeon, Korea, where he is currently working toward the Ph.D. degree in the Department of Electrical Engineering.

His research interests include nanofabrication technology, CMOS characterization, nanobiosensors, conjugated polymer applications, and thermographic imaging.

Jin-Woo Han (S'05–M'10) received the B.S. degree from Inha University, Incheon, Korea, in 2004, and the M.S. and Ph.D. degrees from Korea Advanced Institute of Science and Technology (KAIST), Daejeon, Korea, in 2006 and 2010, respectively.

He is currently a Postdoctoral Fellow with the Center for Nanotechnology, NASA Ames Research Center. He led a research team responsible for developing the unified memory device "Unified-RAM (URAM)" in 2007, the nanoelectromechanical device "Fin Flip-flop Actuated Channel Transistor (FinFACT)" in 2009, and the gateless NPN nanowire device "Bistable Resistor (Biristor)" in 2010. His research interests include novel device and nanofabrication technology, and nanodevices ranging from device design to process development, simulation, characterization, and modeling.

Dr. Han was the recipient of the Best Dissertation Award from KAIST in 2010.

Sung-Jin Choi received the B.S. degree from electronics and electrical engineering from Chung-Ang University, Seoul, Korea, in 2007 and the M.S. degree, in 2008, from Korea Advanced Institute of Science and Technology, Daejeon, Korea, where he is currently working toward the Ph.D. degree in electrical engineering with the Department of Electrical Engineering.

His current research interests include Schottky-barrier devices, capacitorless dynamic random-access memory, biosensors, and nanowire electronics.

Yang-Kyu Choi received the B.S. and M.S. degrees from Seoul National University, Seoul, Korea, in 1989 and 1991, respectively, and the Ph.D. degree from the University of California, Berkeley, in 2001.

He is currently an Associate Professor with the Department of Electrical Engineering, Korea Advanced Institute of Science and Technology. From January 1991 to July 1997, he was with Hynix Semiconductor, Inc., Kyungki, Korea, where he developed 4M, 16M, 64M, and 256M dynamic random-access memories as a Process Integration Engineer. He has also worked on reliability physics and quantum phenomena for nanoscale CMOS. He has authored or coauthored more than 100 papers. He is a holder of seven U.S. patents and 99 Korea patents. His research interests are multiple-gate MOSFETs, exploratory devices, novel and unified memory devices, nanofabrication technologies for bioelectronics, and nanobiosensors.

Dr. Choi was the recipient of the Sakrison Award for the best dissertation from the Department of Electrical Engineering and Computer Sciences, University of California, in 2002, and "The Scientist of the Month for July 2006" from the Ministry of Science and Technology in Korea. His biographic profile was published in the *57th Marquis Who's Who in America*.